Research Article

Relationship among intrinsic magnetic parameters and structure and crucial effect of metastable Fe₃B phase in Fe-metalloid amorphous alloys

Yuanfei Cai [a,c], Bo Lin [b], Yaocen Wang [d], Rie Umetsu [e], Dandan Liang [f], Shoujiang Qu [a,c,*], Yan Zhang [b,*], Junqiang Wang [b,*], Jun Shen [g]

[a] School of Materials Science and Engineering, Tongji University, Shanghai 201804, China
[b] CAS Key Laboratory of Magnetic Materials and Devices and Zhejiang Province Key Laboratory of Magnetic Materials and Application Technology, Ningbo Institute of Materials Technology and Engineering, Chinese Academy of Sciences, Ningbo 315201, China
[c] Shanghai Key Lab. of D&A for Metal-Functional Materials, School of Materials Science & Engineering, Tongji University, Shanghai 201804, China
[d] School of Physical Science and Technology, Northwestern Polytechnical University, Xi'an 710072, China
[e] Institute for Material Research, Tohoku University, Sendai 980-8577, Japan
[f] Shanghai Engineering Research Center of Physical Vapor Deposition (PVD) Superhard Coating and Equipment, Shanghai Institute of Technology, Shanghai 201418, China
[g] School of Materials Science and Engineering, Fujian University of Technology, Fuzhou 350118, China

ABSTRACT

The intrinsic heterogeneity of an amorphous structure originates from composition, and the structure determines the magnetic properties and crystallization models of amorphous magnets. Based on classical Fe–B binary magnetic amorphous alloys, the relationship between the structure and magnetic properties was extensively studied. The stacking structure of Fe–B binary amorphous alloys exhibit discontinuous changes within the range of 74–87 at.% Fe. The structural feature can be expressed as Amor. Fe₃B matrix + Fe atoms are transforming into Amor. Fe matrix + B atoms with the increase of Fe content. The solute atoms are uniformly distributed in the amorphous matrix holes, similar to a single-phase solid solution structure. The transition point corresponds to the eutectic crystallization model composition (Fe₈₂B₁₈ to Fe₈₃B₁₇). A high Fe content will amplify magnetic moment sensitivity to temperature. Under a given service temperature, the disturbance effect of magnetic moment self-spinning will offset the beneficial effect of increasing Fe content and induce the saturation magnetization (M_s) value to decrease. Binary amorphous Fe–B alloys obtain the maximum Curie temperature near 75 at.% Fe, which is slightly smaller than that of the corresponding metastable Fe₃B phase, i.e., the amorphous short-range order structure maintains the highest similarity to the Fe₃B phase. The chemical short-range ordering (SRO) structure of amorphous alloys exhibits heredity to corresponding (meta)stable crystal phases. The unique spatial orientation structure of the metastable Fe₃B phase is the structural origin of the amorphous nature. This study can guide the composition design of Fe-metalloid magnetic amorphous alloys. The design of materials with excellent magnetic properties originates from a deep understanding of precise composition control and temperature disturbance mechanism.

© 2023 Published by Elsevier Ltd on behalf of The editorial office of Journal of Materials Science & Technology.

1. Introduction

Energy structure adjustment proposes more functional requirements for power electronic materials, including magnetism, mechanics, electricity, and optics. The development and use of magnetic materials, including silicon steel, Permalloy, rare-earth permanent magnets, and amorphous–nanocrystalline soft magnets [1–7], accelerate the iterative development of power electronics technology, improve energy conversion efficiency, and reduce invalid energy loss. The magnetic properties of materials are determined through composition, interactions among ferromagnetic atoms (e.g., Fe, Co, and Ni), bonding state, and local coordination environment (ordered periodic lattice or disordered amorphous structure) [8–12]. Given their short preparation process and low

---

no-loading core loss, amorphous soft magnetic materials have been widely used in power transformers, electrical motors, and inductors [13,14].

The structure of amorphous alloys is constructed from polyhedral unit structures with modest topological distortion and chemical disorder [15,16]. The chemical short-range order of metal–metalloid amorphous alloys is close to that of the corresponding crystal structure. Magnetic property is determined by the short-range ordering (SRO) structure, i.e., the exchange integrals (J) between local atom pairs; a positive J induces ferromagnetism, while a negative J induces paramagnetism [17]. The lack of periodic structure does not significantly destroy the intrinsic magnetic moment [10].

An amorphous structure can be continuously adjusted within a specific range of components, and the macroscopic structure still presents a long-range disordered structure. Magnetic properties will undergo apparent changes attributed to SRO change [9,18,19]. Studying ferromagnetic amorphous magnetic parameters can help reveal the evolution of amorphous structures. Another motivation of the present research is that an ultrahigh Fe content will induce the decrease of saturation magnetization (M_s) at room temperature; this phenomenon is universal in different Fe-based amorphous alloys [20], such as FeSiB [21], FeSiBPC [22,23], and FeCoSiBP [24], and FeSiBPCu [25], and the mechanism behind lacks extensive discussion.

In the present research, Fe–B binary magnetic materials were used as the research object, and their major advantage is that amorphous structures can be obtained in a wide range of compositions via melt-quenching [26] or physical vapor deposition (PVD) [27] techniques. The current study systematically researched the magnetic properties and structural transformation of melt-quenched amorphous ribbon with Fe concentration change, while the composition region was Fe_xB_{100-x} (74 at.% $\leq x \leq$ 87 at.%). The measurement of conventional magnetic parameters focuses on the influence mechanism of component alloying on magnetic properties under fixed temperature conditions. However, M_s is a function of temperature, and even a slight temperature perturbation can change the magnetic state [28]. Thus, a single temperature result cannot fully reveal the relationship between composition and magnetic properties. The present work introduced a temperature parameter to characterize the evolution of magnetic materials over a relatively wide temperature range (5 to 350 K). The correlations among atomic magnetic moment, magnetization-temperature (M-T) curve in a low-temperature region, crystallization transition mode, and amorphous stacking form were discussed.

2. Experimental methods

Master alloys with nominal compositions of Fe_xB_{100-x} (74 at.% $\leq x \leq$ 87 at.%) with pure Fe (99.98 mass%) and crystalline B (99.5 mass%) were prepared in a high-frequency induction melting furnace (VF-HMF100, MAKABE, Co., LTD.) in a high-purity Ar atmosphere. Ribbons were prepared using a single copper roller melting-quenching method (VF-RQB20, MAKABE, Co., LTD.) with a width of about 1 mm and a thickness of about 20 μm under a linear rate of 40 m/s. Ultrahigh Fe-based amorphous ribbons (Fe $\geq$ 86 at.%) with a thickness of 16–18 μm were obtained by increasing the linear rate and reducing injecting pressure. Some minor surface crystallization layers were polished with 2000 grit SiC abrasive paper. A similar surface crystallization phenomenon was universal in high-Fe content amorphous systems near the critical glass forming thickness [29]. Prior to magnetic measurements, the amorphous structure was validated via X-ray diffraction (XRD) with Cu $K\alpha$ radiation (D8 Advance, 40 kV and 40 mA, Bruker) from 20° to 90° at a scanning rate of 4°/min. The XRD patterns of the present research can be seen in Fig. S1 in the Supplementary Material. The intrinsic magnetic properties measured with a magnetic property measurement system (MPMS-SQUID, Quantum Design) at an excitation magnetic field of 20 kOe ($\sim$1600 kA/m) are sufficient for Fe-based amorphous alloy saturation. The M_s-T curve is obtained from 5 to 350 K at a continuous heating rate of 0.0833 K/s. Before the heating sequence, the sample is pre-stabilized at 5 K for 5 min, and the intrinsic magnetism at 0 K is derived through curve extrapolation. The thermal physical parameters of the amorphous ribbons were examined via differential scanning calorimetry (DSC, NETZSCH 404C) in a Pt crucible at heating rates of 0.667 and 0.0833 K/s. The lower heating rate can help distinguish crystallization processes with similar kinetic reaction rates. The Curie temperature (T_c) and crystallization temperature (T_x) of the amorphous alloys were derived from DSC heat flow curves. Transmission electron microscopy (TEM, Talos F200) analyses, including selected-area electron diffraction (SAED) and high-resolution TEM (HRTEM), were adopted for microstructure characterization with an acceleration voltage of 200 kV. The TEM samples were prepared via Ar$^+$ ion milling (Gatan 691) on the basis of an as-cast and fully crystallized thin ribbon. The structural information of the stable and metastable phases of the Fe–B binary system was derived from the Materials Project database. Moreover, the visualization of crystal units and XRD pattern simulations were actualized using Visualization for Electronic and Structure Analysis (VESTA) software [30].

3. Results

3.1. Magnetic analysis

The M_s value is an essential parameter for ferromagnetic materials. Moreover, this value is the function of Fe content and service temperature. The diagrams of M_s versus T and M_s versus Fe content at different temperatures of the as-cast Fe_xB_{100-x} (74 at.% $\leq x \leq$ 87 at.%) amorphous alloys are shown in Fig. 1. The external magnetic field is 20 kOe, which is sufficient for the parallel arrangement of magnetic moments. The effective magnetic moment of the ferromagnetic material mainly derives from the spin magnetic moment of unpaired electrons [17]. At a given temperature, the thermodynamic disturbance of temperature is consistent, and the ferromagnetic material will obtain a fixed M_s value. Generally, the M_s value at room temperature is used to evaluate the change of magnetic properties in the composition. With an increase in Fe content, the M_s value under low-temperature conditions exhibits a continuously increasing tendency, but the redistribution of magnetic moments caused by temperature increases accordingly. The M_s value of high Fe-content amorphous samples decays faster at the same temperature interval. A relatively higher Fe content in Fe-based amorphous alloys is the most direct and effective method for improving the M_s of magnetic materials. However, with the enrichment of Fe content, the M_s value cannot maintain a continuously increasing tendency, particularly at higher service temperatures. The disturbance effect of temperature on the magnetic moment is enhanced. The $Fe_{82}B_{18}$ sample can be considered a critical component in the binary system. At 5 K service temperature, a higher Fe content cannot significantly increase the M_s value, and the peak value is about 205 emu/g.

By contrast, at a service temperature of 300 K, a higher Fe content will induce a significantly reduced M_s value. The M_s value of samples with lower Fe content remains nearly unchanged, as shown in Fig. 1(b). Hence, the effect of temperature should not be disregarded. Spin-wave excitation theory [28,31,32] was adopted to describe magnetic behavior at temperatures ranging from 5 to 350 K.

The temperature dependence of magnetization toward 0 K in a ferromagnet (amorphous or crystalline states) is described well by
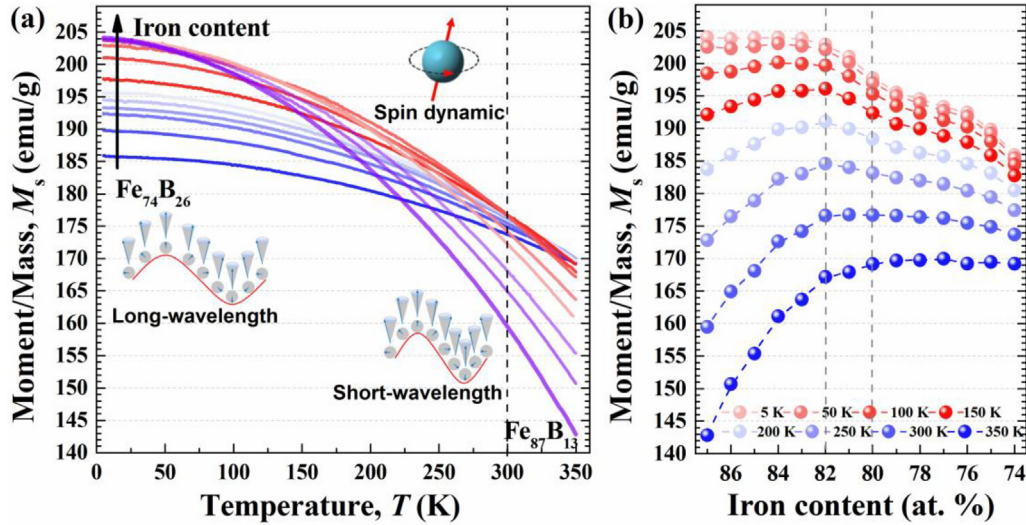
Fig. 1. Variation of M_s with the temperature and composition of as-cast Fe_xB_{100-x} (74 at.% $\leq x \leq$ 87 at.%) amorphous ribbons at an external magnetic field of 20 kOe. (a) Magnetization-temperature (M_s-T) curves of as-cast amorphous ribbons. The insets show diagrams of the electron magnetic moment being disturbed by temperature. (b) Relationship between M_s and Fe content at different service temperatures.

Bloch's $T^{3/2}$ law, which indicates that long-wavelength spin wave excitations determine magnetization behavior. Spin-wave energies are described well by the following quadratic dispersion relation [33]:

$$E_q = D\left(q^2 - \frac{\langle r^2 \rangle}{20}q^4 + \dots\right) + 2\pi\mu_B g M_0 \langle \sin^2\theta \rangle, \qquad (1)$$

where D is the stiffness parameter, and $\langle r^2 \rangle$ is the second moment of the exchange interaction defined by

$$\langle r^2 \rangle = \frac{\int J(r)g(r)r^4 dr}{\int J(r)g(r)r^2 dr}, \qquad (2)$$

where $J(r)$ is the exchange interaction, and $g(r)$ is the pair correlation function. The constant term in Eq. (1) is an effective (pseudo-) gap in the spin-wave dispersion relation due to dipolar interactions, θ is the polar angle of the wave vector (the z-axis is defined as the direction of spontaneous magnetization), and $\langle \sin^2\theta \rangle$ denotes the average over all magnetic domains. The spontaneous magnetization $M(T)$ at low temperatures can be described by [34]

$$M(T) = M(0)\left(1 - BT^{3/2} - CT^{5/2} - \dots\right), \qquad (3)$$

where coefficients B and C are related to coefficients q^2 and q^4 in Eq. (1), respectively. At extremely low temperatures, the single $T^{3/2}$ term is sufficient to describe the magnetization behavior, i.e., Bloch's $T^{3/2}$ law, which is frequently described as a "long-wavelength spin wave." As temperature increases, spin-wave interactions should be considered, and "short-wavelength spin wave" will be excited, referring to the term $T^{5/2}$. In the present research, the two parts of Eq. (3) can fit the M_s-T curve well by using Origin software. This condition is sufficient for Fe–B amorphous alloys in the 5–350 K region.

The spin-wave parameters B and C of amorphous alloys with different Fe contents are plotted in Fig. 2 to describe the M_s-T behavior of the other amorphous structures. A higher value indicates that M_s decreases faster with temperature disturbance. Furthermore, the spin-wave stiffness parameter D will be calculated on the basis of parameters B and C in our future manuscript. This topic is not covered in the present study. As shown in Fig. 2, as Fe content decreases, parameters B and C tend to decrease gradually, and the parameters are sensitive to the structural differences of ferromagnetic materials. The reduction rate shifts to a relatively
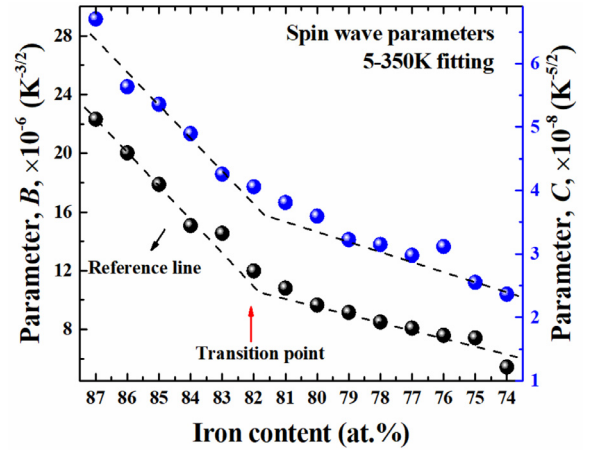
Fig. 2. Spin wave parameters B and C of the amorphous ribbons vs. Fe content are obtained via nonlinear fitting of the M_s-T curves from 5 to 350 K on the basis of Bloch's equation.

lower value when Fe content is lower than 82 at.%. This result has not been reported in previous research, and the shift should originate from a transition in the amorphous structure before and after the critical composition, i.e., $Fe_{82}B_{18}$. The relation between an amorphous structure and magnetic properties is a crucial scientific question.

The average magnetic moment ($\bar{\mu}$) can be derived from the following equation [37]:

$$\bar{\mu} = \frac{M_s(0)M_{mol}}{N\mu_B}, \qquad (4)$$

where M_{mol} is the molecular weight, N is Avogadro's constant, μ_B is the number of Bohr magnetons, and $M_s(0)$ is the spontaneous magnetization intensity at 0 K. Fig. 3 shows the moment per Fe atom ($\bar{\mu}_{Fe}$) versus Fe content relationship, and the maximum value can be obtained between 84 at.% and 85 at.%. Further increasing Fe content will lead to intrinsic magnetic moment attenuation. The dashed line in Fig. 3 is the extrapolated guideline, and the extrapolated amorphous pure Fe (Amor. Fe) is about 1.4 μ_B. The relevant theoretical calculation results show that when binary amorphous Fe–B is about Fe=85 at.%, the intrinsic magnetic moment value
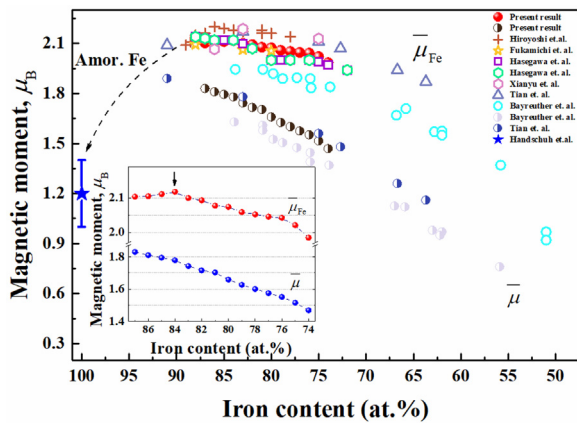
Fig. 3. Intrinsic magnetic moment of per Fe atom ($\bar{\mu}_{Fe}$) and per atom ($\bar{\mu}$) of the as-cast Fe–B binary amorphous ribbons and films as a function of Fe content at 0 or 4.2 K. The results of different groups were summarized in [27,32,35-40]. The inset is the result of the present research. The dashed line indicates a downward trend toward ideal amorphous Fe in the Fe-metalloid system.

reaches the maximum value of about 2.17 μ_B [41] and then decreases significantly. The present result finds the maximum value at 84 at.% Fe content, and the magnetic moments exhibit a certain discreteness derived from different groups.

The amorphous Fe interlayer can grow into an amorphous structure until a critical thickness of about 2 nm on amorphous Dy [42], Gd [43], or Y [44] substrates prepared via evaporation in an ultrahigh vacuum on GaAs (100) and quartz glass substrates. The amorphous structure can remain stable at room temperature. The average magnetic moments of these amorphous Fe films are strongly reduced to (1.2 ± 0.2) μ_B, while T_c is reduced to (80 ± 3) K. Conversely, in the conventional bulk body-centered cubic (BCC) Fe, the moment per atom is 2.2 μ_B, and T_c is 1073 K. The structure of pure amorphous Fe obtained by extrapolating Fe-metalloid and Fe-Zr (transition group metals) is not unique [45]. Similar to the face-centered cubic (FCC) Fe system and the magnetic state nonuniqueness obtained via extrapolation, it is primarily determined by its average atomic volume. Moreover, the change in local stacking structure will form a mutual transition among ferromagnetic, paramagnetic, and spin glass states. The local structure of pure Amor. Fe does not inherit its local configuration from the BCC Fe crystal unit and ultrahigh Amor. Fe content is not beneficial to improve the intrinsic magnetic moment.

3.2. Thermodynamic analysis

Fig. 4 shows the DSC curves of Fe_xB_{100-x} (74 at.% ≤ x ≤ 87 at.%) amorphous alloy at different heating rates. It involves the exothermic peaks of crystallization and the endothermic peaks of ferromagnetic-to-paramagnetic transformation in the baseline curves. A low heating rate (0.0833 K/s-5 K/min) is adopted to distinguish exothermic reactions with close crystallization kinetics. The exothermic crystallization peak of Fe_xB_{100-x} (77 at.% ≤ x ≤ 81 at.%) at a heating rate of 0.0833 K/s, shown in Fig. 4(a), is divided into two exothermic peaks that correspond to the eutectic reaction and polymorphic transition reaction of the residual amorphous structure, respectively. A typical exothermic peak of $Fe_{77}B_{23}$ sample at 0.0833 K/s is shown in Fig. 4(d). As heating rate increases, the two-step crystallization reaction will coincide, as illustrated in Fig. 4(b). Fig. 4(c) depicts the second scanning baseline curve. The samples are first heated to 1073 K at 0.667 K/s and then furnace-cooled to room temperature. The endothermic peak of the T_c point identifies the crystallization products. T_c value

significantly differs among metastable Fe_3B, stable Fe_2B, and α-Fe phases [26].

As Fe content gradually increases from 76 at.% to 84 at.%, the relative intensity of the endothermic peak of the α-Fe phase gradually increases, and the crystallization product transforms from a single metastable Fe_3B to a two-phase mixture. Simultaneously, the metastable Fe_3B phase is proven not to undergo significant decomposition during DSC heating. This phase can remain stable at room temperature. However, the metastable Fe_3B phase formed in the $Fe_{75}B_{25}$ sample will decompose to stable α-Fe and Fe_2B phases at around 980 K during heating at a rate of 0.667 K/s. Exothermic enthalpy is about 4.87 J/g. The multistep DSC scanning curves of the $Fe_{75}B_{25}$ sample are shown in Fig. S2 in the Supplementary Material. The sample is transformed into a metastable Fe_3B phase of the same composition by the polymorphic crystallization model.

Increasing Fe content will improve stability of the metastable Fe_3B phase formed during amorphous crystallization. Possible reasons for increased strength may be the precipitation of the minor α-Fe phase around Fe_3B grains or the crystal structure of metastable Fe_3B phase has changed, improving the solid-state phase transition barrier. When Fe content exceeds 83 at.%, the crystallization peak splits into two apparent peaks. The first peak corresponds to the precipitation of α-Fe phase, indicating that the concentration of Fe atoms in amorphous state is excessive. Fe atoms preferentially aggregate at a lower temperature during heating. When Fe content reaches 85 at.%, the crystallization products are stable α-Fe and Fe_2B phases. The amorphous matrix gradually changes from pure Amor. Fe_3B structure to Amor. Fe structure with increased Fe concentration. The emergence of a primary crystalline structure indicates that the Amor. Fe structural units occupy a dominant position. The short-range structure in amorphous state is inherited from the corresponding stable or metastable crystalline structure.

Activation energy of the first onset crystallization peak (E_{x1}) of different samples was calculated using the Kissinger method [46]. The equation is

$$\ln\left(T^2/\beta\right) = \ln(E/R) - \ln\nu + E/RT, \tag{5}$$

where T is the specific temperature (K), β is heating rate (K/s), E is activation energy (kJ/mol), R is gas constant (8.3145 J/(mol K)), and ν is frequency factor. Fig. 4(e) presents activation energy results versus Fe content. When Fe content is more than 83 at.%, E_{x1} decreases linearly with an increase in Fe content, corresponding to the primary crystallization model. The $Fe_{82}B_{18}$ and $Fe_{83}B_{17}$ samples exhibit higher crystallization resistance. The rearrangement of atoms requires more energy in the eutectic crystallization model. When Fe content is lower than 82 at.%, the E_{x1} value of different samples is nearly the same, possibly indicating that the crystal's initial nucleus is similar. On the basis of the DSC result, the amorphous structure of Fe_xB_{100-x} (74 at.% ≤ x ≤ 87 at.%) can be divided into two parts: Amor. Fe matrix and Amor. Fe_3B matrix. The critical composition is $Fe_{82}B_{18}$.

3.3. Microstructure analysis of amorphous and crystal Fe_3B phase

We analyzed the microstructure of the $Fe_{76}B_{24}$ samples, including the as-cast and 883 K-10 min annealing state, as shown in Fig. 5. Fig. 5(a) shows the BF image of the as-cast $Fe_{76}B_{24}$ sample, which exhibits typical homogeneous contrast without evident ordered lattice fringes. The corresponding SAED in Fig. 5(e) presents the diffraction pattern with two dispersed diffraction halos without detectable diffraction spots. The microstructure and diffraction pattern of the fully crystallized $Fe_{76}B_{24}$ sample (883 K-10 min) are shown in Fig. 5(b, f), respectively. Crystalline size distribution is about 50–150 nm. The diffraction ring acquisition area is a circular region with a diameter of about 850 nm. It contains about 50 spa-
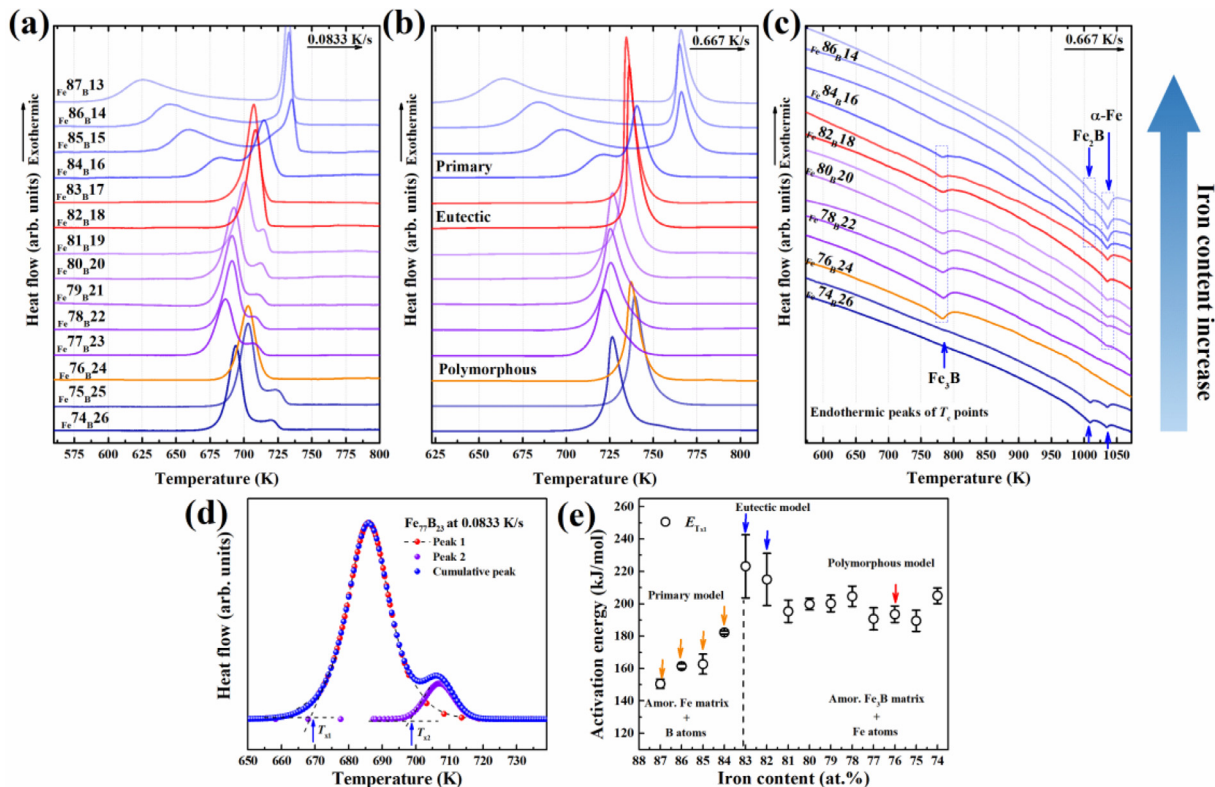
Fig. 4. DSC curves of Fe_xB_{100-x} (74 at.% $\leq x \leq$ 87 at.%) with different heating rates: (a) 0.0833 K/s and (b) 0.667 K/s. (c) Second scanning curve of the sample's baseline after first scanning to 1073 K at 0.667 K/s and furnace cooling to room temperature. The type of crystalline phases and relative content can be determined by the characteristic endothermic peak and enthalpy, respectively. (d) A typical mixed crystallization peak of $Fe_{77}B_{23}$ amorphous sample involves two divided crystallization sequences that can be separated under a low heating rate. (e) Activation energy (E_{x1}) of the onset temperature of the first crystallization peak (T_{x1}) on the basis of the Kissinger method.

tially randomly oriented Fe_3B grains. The bright diffraction spots in Fig. 5(f) are distributed within a certain range derived from the special lattice structure of the Fe_3B phase.

From the database of Materials Project [50], we can derive detailed structural information of metastable Fe_3B. The system recorded number is mp-1181327, which corresponds to PDF# 39-1316 (tetragonal I$\bar{4}$, 82) in the MDI Jade 6.5 database. The crystal structure has three inequivalent Fe sites. In the first Fe site, Fe is bonded in a two-coordinate geometry to two equivalent B atoms, including one shorter (2.13 Å) and one longer (2.23 Å) Fe–B bond length. In the second Fe site, Fe is bonded in a three-coordinate geometry to three equivalent B atoms, exhibiting a spread of Fe–B bond distances ranging from 2.12 to 2.31 Å. In the third Fe site, Fe is bonded in a four-coordinate geometry to four equivalent B atoms, exhibiting a spread of Fe–B bond distances ranging from 2.18 to 2.21 Å, and a B atom is bonded in a nine-coordinate geometry to nine Fe atoms. A spread of covalent-like Fe–B bond distances is similar to the amorphous structure, which exhibits a distribution of nearest-neighbor environments and bond lengths for a given atom and can be described by the radial distribution function and a higher-order correlation function [17]. The feature of the metastable Fe_3B may be the intrinsic structure factor for the system that can be quenched into a stable amorphous alloy.

If the grain size of the Fe_3B phase is reduced to nanoscale particles, then the diffraction pattern of the sample will become more diffused and similar to an amorphous type, i.e., Fig. 5(f) transforms into Fig. 5(e). The structural similarity indicates the minimal difference between the metastable Fe_3B and the corresponding amorphous state. The structural similarity should be the structural origins of this binary system, which can be quenched into an amorphous state. Fig. 5(c) shows the HRTEM image of a sin-

gle Fe_3B particle ([$Z = [\bar{1}00]$). The FFT image of Fig. 5(c) is shown in Fig. 5(g), presenting periodic diffraction spots. The atomic number of the B atom is significantly lower than that of the Fe atom. Hence, the bright atomic layer in Fig. 5(c) should correspond to the Fe atom layer. The atomic structure distribution in the simulated crystal structure of Fe_3B is shown in Fig. 5(d). The exact orientation in Fig. 5(c) is maintained, and the related Miller indexes are annotated on the figures. Fig. 5(i) shows the radial intensity profiles of the as-cast amorphous and fully crystallized state, corresponding to Fig. 5(e, f), respectively. Fig. 5(j) shows XRD patterns of the as-cast $Fe_{76}B_{24}$ sample and the simulated powder diffraction patterns of possible phases. The prominent diffraction peaks of the metastable Fe_3B exhibit a distribution of the Miller index of possible spatial configuration that corresponds to the diffuse diffraction peak of the amorphous structure. The Fe_3B structural units prefer to form disordered amorphous structures, and Fe–B atoms can also establish covalent-like bonds, forming chemical SRO (CSRO) structures. The structure of Fe_xB_{100-x} (74 at.% $\leq x \leq$ 81 at.%) binary amorphous alloys can be depicted as spatially randomly distributed Fe_3B unit cells that connect additional Fe atoms.

### 3.4. Curie temperature and average atomic volume versus Fe content

Fig. 6 shows T_c and average atomic volume (V_m) as functions of Fe content. Both variables present a break in the slope around the $Fe_{82}B_{18}$ sample, consistent with the result in Fig. 2. The amorphous structure transformation induces nonlinear changes in magnetic properties. In accordance with molecular field theory, T_c can be expressed by the following equation [26]:

$$T_C = \frac{2z_{av}J_{Fe-Fe}S(S+1)}{3k_B},\tag{6}$$
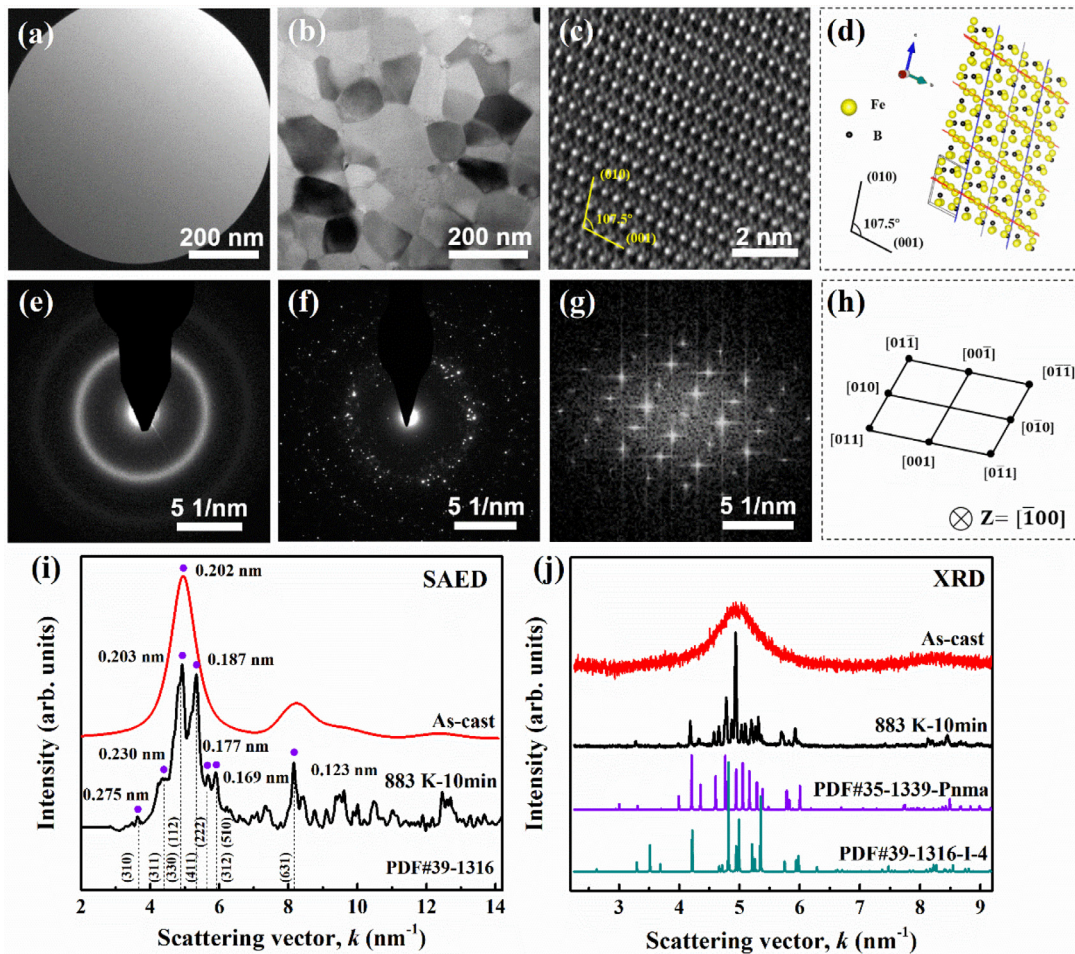
Fig. 5. Microstructure analysis of the $Fe_{76}B_{24}$ sample at the amorphous and fully crystallized states: (a) Bright field image (BF) of the as-cast amorphous state, (b) BF of the sample annealed at 883 K for 10 min, (c) HRTEM of a single metastable Fe_3B particle, and (d) schematic graph of the projection of the unit structure of $I\bar{4}$ type Fe_3B in $[\bar{1}00]$ direction, corresponding to the 2D diffraction pattern in (c). (e) SAED of Fig. (a). (f) SAED of (b). (g) Fast Fourier transform (FFT) image of (c). (h) Schematic graph of the diffraction pattern that corresponds to (g), with the electron beam direction along $[\bar{1}00]$. (i) Radial intensity profile of the as-cast amorphous and fully crystallized states, corresponding to (e, f), respectively. 1D data are obtained through the azimuthal integration of the 2D diffraction pattern in PASAD tools v3.0 [47], a plug-in of Digital Micrograph software 3.21. (j) Conventional XRD patterns and simulated polycrystalline diffraction patterns of possible Fe_3B phases. The diffraction angle 2θ is converted into the scattering vector k in the reciprocal space by using $k = 1/d = 2\sin\theta/\lambda$. Then, the momentum vector $\boldsymbol{q}$ can be calculated using $q = 4\pi\sin\theta/\lambda = 2\pi k$, where λ is the X-ray wavelength of Cu $K\alpha$=1.54056 Å, and d is the lattice spacing [48,49].
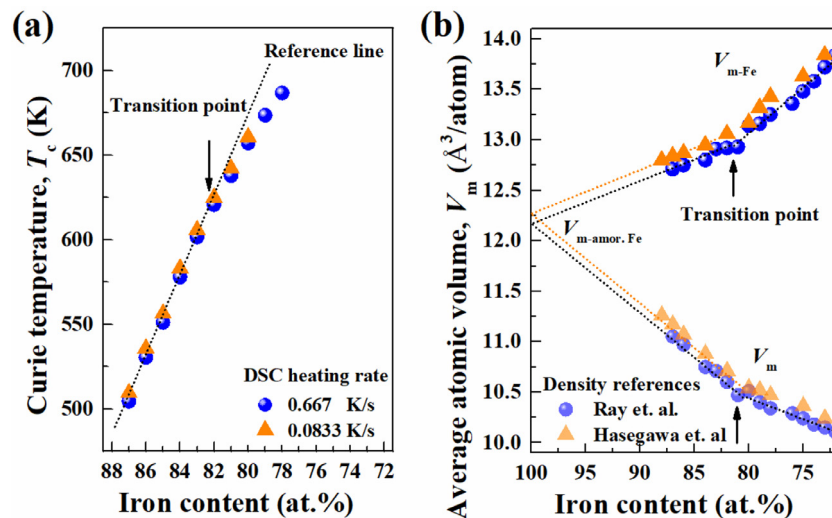
Fig. 6. (a) T_c vs. Fe content obtained via DSC. The yellow points (triangle) correspond to T_c measured at a heating rate of 0.0833 K/s. The blue points (sphere) correspond to T_c measured at a heating rate of 0.667 K/s. The former is slightly higher than the latter, with more relaxation time during heating. (b) Average atomic volume per atom of the as-cast Fe–B binary amorphous ribbons based on ribbon density data and derived from the literature [37,51].
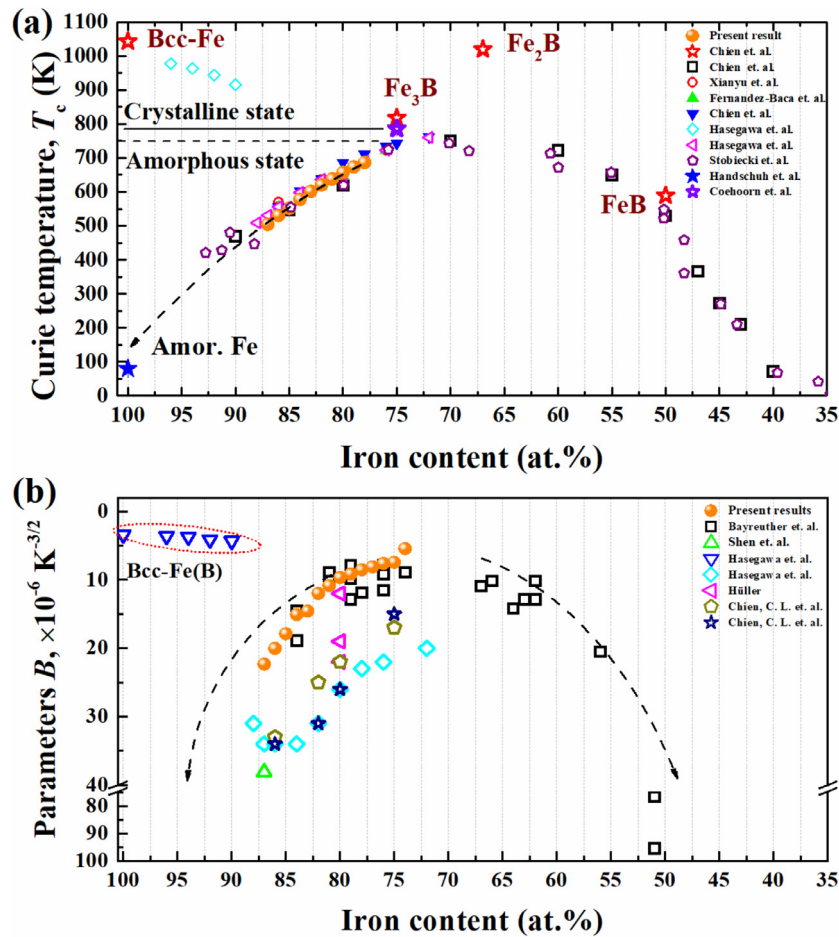
Fig. 7. (a) T_c of amorphous Fe_xB_{100-x} ribbons, amorphous films, and metastable and stable crystalline Fe–B compounds. Some data are derived from the literature [26,27,32,33,44,59-61]. (b) A summary of spin-wave parameters B in Fe–B binary amorphous and metastable phases exhibits certain discreteness derived from measurement equipment and curve fitting method. It exhibits a negative correlation with Curie T_c vs. Fe content in (a) [26,28,32,40,62].

where S is spin quantum number, J_{Fe-Fe} is exchange integrals that is determined by the atomic spacing of Fe–Fe atomic pairs, z_{av} is local coordination number, and k_B is Boltzmann constant. In the aspect of atomic environment, atomic volume is determined by the nearest atomic spacing (d) and local coordination number. Given the lack of long-range translational or orientational order in amorphous alloys, V_m can be used to describe structure-property relationship. A power-law correlation function over the medium-range order has been proven in metal-metal glasses [48]. Thus, the parameter V_m of per atom and Fe atom is adopted to discuss the structure-magnetic property relationship, and they can be calculated using the following equation [52,53]:

$$V_{m-Fe} = 100 \cdot \frac{V_m}{x} = 100 \cdot \frac{M_{mol}}{x \cdot \rho}, \qquad (7)$$

where V_{m-Fe} is average atomic volume per Fe atom, V_m is average atomic volume per atom, x is the Fe content in Fe_xB_{100-x} amorphous alloys, M_{mol} is the molecular weight, and ρ is mass density of the amorphous sample as derived from the literature [37,51]. Densities of the master ingots in the present research and the as-cast ribbon are plotted in Fig. S3 in the Supplementary Material. The nonlinear change in V_m is favorable evidence for transforming the amorphous stack structure with increased Fe content. The V_m of a single solid solution in crystalline materials that vary with solute content increases and exhibits segmented linear changes when multiple terminal solid solutions exist [54]. Fe_xB_{100-x} (74 at.% ≤ x ≤ 87 at.%) binary amorphous alloys trans-

form amorphous stacking structure around the $Fe_{82}B_{18}$ sample. The primary and polymorphous crystallization samples correspond to two types of amorphous structures. The classification of Amor. Fe and Amor. Fe_3B can also be verified from the thermal analysis results, as shown in Fig. 4. The structural model of Amor. Fe can be described as Bernal dense random packing (DRP) of the hard sphere [55]. Polk [56] indicated that a DRP metal atom framework that contains metalloid atoms in all the large "interstitial" holes would compose 21 at.% metalloid and 79 at.% metal. The DRP model considers the interaction between metal and metalloid atomic pair, and critical composition may deviate from the ideal state. The short-range in amorphous systems can be classified into two types, i.e., topological (physical) SRO and compositional (chemical) CSRO [57], which may correspond to the Amor. Fe and Amor. Fe_3B matrix, respectively.

4. Discussion

Composition determines the structure and induces changes in physical and chemical properties. Magnetic properties are susceptible to minor changes in local structure, and the structure of ferromagnetic amorphous materials can be analyzed via systemic characterization of magnetic parameters. Based on the analysis of the intrinsic magnetic properties, crystallization transition behavior, and polymorphous transition of the metastable Fe_3B phase, Fe_xB_{100-x} (74 at.% ≤ x ≤ 87 at.%) amorphous alloys exhibit an

amorphous stacking structure transition, i.e., from Amor. Fe₃B to Amor. Fe-based amorphous structure. Subsequently, the variation in intrinsic magnetic properties of Fe–B binary amorphous structures can be discussed in a broader composition region. As mentioned above, T_c is a function of the local coordination of magnetic atoms and is sensitive to minor variations of the local structure.

The T_c exhibits a roughly linear relationship with spin-wave stiffness constant D [58], which can be calculated from the spin-wave parameter B. The magnetic parameters B and T_c describe the sensitivity of magnetic moment to temperature, corresponding to low-temperature and high-temperature regions, respectively. The present results and related data derived from the literature are plotted in Fig. 7. On a broader composition range, T_c exhibits a trend of initially increasing and then decreasing with an increase in Fe content, whereas parameter B exhibits a tendency of initially decreasing and then increasing. The extreme value is around $Fe_{75}B_{25}$ (Fe₃B). The local exchange interaction achieves the highest value, which may be derived from the CSRO structure of Fe–B atomic bonds. The structure of amorphous alloys creates topological disorder and chemical disorder, which correspond to Amor. Fe and Amor. Fe₃B local structural units in the present Fe–B system, respectively. The CSRO of metal-metalloid amorphous alloys is close to that of the corresponding crystal structure, and similar local structures induce nearly identical T_c point.

On the Fe-rich side, the higher the Fe content, the lower the T_c. When Fe content is higher than 82 at.%, T_c attenuation rate increases with an increase in Fe content, as shown in Fig. 6. The spin-wave parameter B in Fig. 2 presents a consistent transition law. That is when an amorphous stack structure changes into an Amor. Fe-based amorphous structure, the sensitivity of magnetic moment to temperature increases. Consequently, the M_s value of amorphous samples exhibits an apparent decrease in the high Fe content region (>82 at.%) at room temperature, as shown in Fig. 1(b). During M_s-T curve fitting, the $T^{3/2}$ and $T^{5/2}$ terms (Eq. (3)) are considered simultaneously, that is, the "short-wavelength spin-wave" part is considered in the 5–350 K temperature region. The present result is consistent with that of Bayreuther et al. [40], who also assumed the $T^{5/2}$ term. The values from other groups [26,28,32,62] will be checked and discussed in our future research, which is meaningful for Fe-metalloid amorphous alloys.

5. Conclusions

In summary, the change in the intrinsic magnetic properties of ferromagnetic amorphous alloys originates from the amorphous stacking structure. The CSRO structure of amorphous alloys exhibit structural heredity to corresponding (meta)stable crystal phases. We can draw the following conclusions from analyzing M_s-T curves, DSC, and TEM of Fe–B binary amorphous ferromagnetic alloys:

(1) The amorphous stacking structure exhibits a break in the matrix near the eutectic composition, and the enrichment of Fe content induces lower T_c and relatively lower M_s at room temperature.

(2) The Fe_xB_{100-x} (74 at.% $\leq x \leq$ 87 at.%) binary amorphous alloys comprise two structural units: Bernal-type Amor. Fe matrix and CSRO Amor. Fe₃B matrix. The Amor. Fe matrix + B atoms alloys, corresponding to the primary crystallization model, can more easily excite "short-wavelength spin wave" and increase the sensitivity of M_s to temperature.

(3) The M_s value refers to the balance of intrinsic magnetic moment and stability versus temperature. The unique Fe–B bond pair distribution feature of the metastable Fe₃B phase may be the structural origin of amorphous nature.

Declaration of Competing Interest

The authors declare that they have no known competing financial interests or personal relationships that could have appeared to influence the work reported in this paper.

Supplementary materials

Supplementary material associated with this article can be found, in the online version, at doi:10.1016/j.jmst.2023.07.079.

References

[1] M.A. Willard, M. Daniil, K.E. Kniping, Scr. Mater. 67 (2012) 554–559.
[2] J.M. Silveyra, E. Ferrara, D.L. Huber, T.C. Monson, Science 362 (2018) eaao0195.
[3] T. Egami, Rep. Prog. Phys. 47 (1984) 1601–1725.
[4] C.D. Graham, T. Egami, Ann. Rev. Maler. Sci. 8 (1978) 423–457.
[5] R. Hasegawa, J. Magn. Magn. Mater. 41 (1984) 79–85.
[6] J.M.D. Coey, J. Alloy. Compd. 326 (2001) 2–6.
[7] Y. Zhang, P. Sharma, A. Makino, IEEE Trans. Magn. 50 (2014) 4.
[8] J.M.D. Coey, J. Appl. Phys. 49 (1978) 1646–1652.
[9] I. Vincze, D.S. Boudreaux, M. Tegze, Phys. Rev. B 19 (1979) 4896–4900.
[10] A.I. Gubanov, Sov. Phys. Solid State 2 (1960) 468–471.
[11] F.E. Luborsky, J. Magn. Magn. Mater. 7 (1978) 143–149.
[12] P.B. Chen, T. Liu, F.Y. Kong, A.D. Wang, C.Y. Yu, G. Wang, C.T. Chang, X.M. Wang, J. Mater. Sci. Technol. 34 (2018) 793–798.
[13] R. Hasegawa, J. Magn. Magn. Mater. 100 (1991) 1–12.
[14] Y. Ogawa, M. Naoe, Y. Yoshizawa, R. Hasegawa, J. Magn. Magn. Mater. 304 (2006) E675–E677.
[15] J.J. Gilman, Phys. Today 28 (1975) 46–53.
[16] J.J. Gilman, Philos. Mag. B 37 (1978) 577–584.
[17] J.M.D. Coey, Magnetism and Magnetic Materials, Cambridge University Press, 2010.
[18] Y. Waseda, H. Okazaki, T. Masumoto, J. Mater. Sci. 12 (1977) 1927–1949.
[19] X. Tong, Y. Zhang, Y.C. Wang, X.Y. Liang, K. Zhang, F. Zhang, Y.F. Cai, H.B. Ke, G. Wang, J. Shen, A. Makino, W.H. Wang, J. Mater. Sci. Technol. 96 (2022) 233–240.
[20] B. Huang, Y. Yang, A.D. Wang, Q. Wang, C.T. Liu, Intermetallics 84 (2017) 74–81.
[21] S.Q. Yue, H. Zhang, R.J. Cheng, A.D. Wang, Y.Q. Dong, A.N. He, H.W. Ni, C.T. Liu, J. Alloy. Compd. 776 (2019) 833–838.
[22] P.B. Chen, A.D. Wang, C.L. Zhao, A.N. He, G. Wang, C.T. Chang, X.M. Wang, C.T. Liu, Sci. China-Phys. Mech. Astron. 60 (2017) 6.
[23] Y. Han, F.L. Kong, C.T. Chang, S.L. Zhu, A. Inoue, E.S. Shalaan, F. Al-Marzouki, J. Mater. Res. 30 (2015) 547–555.
[24] Y. Han, J. Ding, F.L. Kong, A. Inoue, S.L. Zhu, Z. Wang, E. Shalaan, F. Al-Marzouki, J. Alloy. Compd. 691 (2017) 364–368.
[25] A. Makino, H. Men, K. Yubuta, T. Kubota, J. Appl. Phys. 105 (2009) 013922.
[26] C.L. Chien, D. Musser, E.M. Gyorgy, R.C. Sherwood, H.S. Chen, F.E. Luborsky, J.L. Walter, Phys. Rev. B 20 (1979) 283–295.
[27] T. Stobiecki, F. Stobiecki, J. Magn. Magn. Mater. 35 (1983) 217–218.
[28] K. Hüller, J. Magn. Magn. Mater. 61 (1986) 347–358.
[29] T. Liu, A.N. He, F.Y. Kong, A.D. Wang, Y.Q. Dong, H. Zhang, X.M. Wang, H.W. Ni, Y. Yang, J. Mater. Sci. Technol. 68 (2021) 53–60.
[30] K. Momma, F. Izumi, J. Appl. Cryst. 44 (2011) 1272–1276.
[31] F. Bloch, Z. Phys. 61 (1930) 206–219.
[32] R. Hasegawa, R. Ray, Phys. Rev. B 20 (1979) 211–214.
[33] J.A. Fernandez-Baca, J.W. Lynn, J.J. Rhyne, G.E. Fish, Phys. Rev. B 36 (1987) 8497–8511.
[34] S.N. Kaul, P.D. Babu, Phys. Rev. B 50 (1994) 9308–9322.
[35] H. Hiroyoshi, K. Fukamichi, A. Kikuchi, A. Hoshi, T. Masumoto, Phys. Lett. A 65 (1978) 163–165.
[36] K. Fukamichi, M. Kikuchi, S. Arakawa, T. Masumoto, Solid State Commun. 23 (1977) 955–958.
[37] R. Hasegawa, R. Ray, J. Appl. Phys. 49 (1978) 4174–4179.
[38] Z. Xianyu, Y. Ishikawa, T. Fukunaga, N. Watanabe, J. Phys. F 15 (1985) 1799–1812.
[39] H. Tian, C. Zhang, J.J. Zhao, C. Dong, B. Wen, Q. Wang, Physica B 407 (2012) 250–257.
[40] G. Bayreuther, G. Enders, H. Hoffmann, U. Korndörfer, W. Oestreicher, K. Röll, M. Takahashi, J. Magn. Magn. Mater. 31–34 (1983) 1535–1536.
[41] J. Hafner, M. Tegze, Ch. Becker, Phys. Rev. B 49 (1994) 285–298.

[42] K. Yoden, N. Hosoito, K. Kawaguchi, K. Mibu, T. Shinjo, Jap. J. Appl. Phys. 27 (1988) 1680.

[43] J. Landes, Ch Sauer, B. Kabius, W. Zinn, Phys. Rev. B 44 (1991) 8342–8345.

[44] S. Handschuh, J. Landes, U. Köbler, Ch. Sauer, G. Kisters, A. Fuss, W. Zinn, J. Magn. Magn. Mater. 119 (1993) 254–260.

[45] G. Xiao, C.L. Chien, Phys. Rev. B 35 (1987) 8763–8766.

[46] H.E. Kissinger, Anal. Chem. 29 (1957) 1702–1706.

[47] C. Gammer, C. Mangler, C. Rentenberger, H.P. Karnthaler, Scr. Mater. 63 (2010) 312–315.

[48] D. Ma, A.D. Stoica, X.L. Wang, Nat. Mater. 8 (2009) 30–34.

[49] J. Bednarčík, S. Michalik, V. Kolesar, U. Rutt, H. Franz, Phys. Chem. Chem. Phys. 15 (2013) 8470–8479.

[50] The Materials Project. Materials Data on Fe3B by Materials Project, 2020, 10.17188/1663470.

[51] R. Ray, R. Hasegawa, C.P. Chou, L.A. Davis, Scr. Metall. 11 (1977) 973–978.

[52] A.R. Yavari, J. Mater. Res. 1 (1986) 746–751.

[53] P.H. Gaskell, Acta Metall. 29 (1981) 1203–1211.

[54] I. Bakonyi, Acta Mater. 53 (2005) 2509–2520.

[55] J.D. Bernal, Nature 185 (1960) 68–70.

[56] D.E. Polk, Scr. Metall. 4 (1970) 117–122.

[57] Y. Waseda, H.S. Chen, Sci. Rep. Res. Inst. Tohoku Univ. 28 (1980) 143–155.

[58] F.E. Luborsky, J.L. Walter, H.H. Liebermann, E.P. Wohlfarth, J. Magn. Magn. Mater. 15–18 (1980) 1351–1354.

[59] C.L. Chien, K.M. Unruh, Phys. Rev. B 24 (1981) 1556–1558.

[60] Z. Xianyu, Y. Ishikawa, S. Ishio, M. Takahashi, J. Phys. F 15 (1985) 1787–1797.

[61] R. Coehoorn, D.B. de Mooij, C. de Waard, J. Magn. Magn. Mater. 80 (1989) 101–104.

[62] B.G. Shen, W.S. Zhan, J.G. Zhao, J.C. Chen, Acta Phys. Sin. 34 (1985) 1009–1015.